Organization of cyanobiphenyl liquid crystal molecules in prewetting films spreading on silicon wafers

S. Bardon, R. Ober, M. P. Valignat, F. Vandenbrouck, and A. M. Cazabat
Laboratoire de Physique de la Matière Condensée, Collège de France, 11 Place Marcelin Berthelot, 75231 Paris, France

J. Daillant
Service de Physique de l'Etat Condensé, Orme des Merisiers CEA Saclay, 91197 Gif sur Yvette, France
(Received 18 August 1998; revised manuscript received 16 February 1999)

We observe prewetting films of 8CB (4′-*n*-octyl-4-cyanobiphenyl) spreading at room temperature on silicon wafers by ellipsometry and x-ray reflectivity. Ellipsometry indicates the formation of a nondense monolayer spreading in front of a 45-Å-thick film. X-ray reflectivity, performed using a ribbon geometry for the liquid crystal (LC) reservoir, allows us to determine the organization of the 8CB molecules in the homogenous film. It consists of a trilayer stacking with a smecticlike bilayer standing above a polar monolayer with tilted molecules. We show that the thickness of the bilayer is equal to the smectic periodicity in the bulk material and that the tilt angle of the molecules in contact with the solid surface is close to 60°, in good agreement with second-harmonic generation studies reported by other groups. Such organization can be precisely determined using x-ray reflectivity because it induces a modulation of the electron density along the normal to the surface. Furthermore, a study of the ellispometric profile of a drop heated in the nematic phase, where we observe a complete spreading of the LC, shows the complex structuration of the LC close to the solid interface. In particular, the spreading behavior of the trilayer compared to the subsequent smecticlike bilayers indicates the existence of specific interaction between the trilayer and silicon wafer. [S1063-651X(99)06106-1]

PACS number(s): 64.70.Md, 61.30.−v

I. INTRODUCTION

The interaction of liquid crystals (LC's) with solid surfaces has attracted considerable attention both in fundamental and applied research [1–3]. On the one hand, LC's exhibit various kinds of surface ordering and surface transitions which are far from being completely understood. On the other hand, alignment layers are key components of liquid crystal displays and, despite a large research effort, the molecular mechanism of bulk anchoring to a surface remains unclear.

In this respect, the organization of the LC molecules in first layers at interfaces is of special interest. Research has been carried out to study the organization of LC molecules on solid surfaces using optical microscopy [4], x-ray reflectivity [5,6], ellipsometry [6,7], second-harmonic generation [8,9], scanning probe microscopy [10,11], and Fourier transform infrared spectroscopy [12]. Most of these techniques have also been used to study Langmuir films of liquid crystals [13–16]. In this paper, we describe the use of ellipsometry and x-ray reflectivity to study the arrangement of 4′-*n*-octyl-4-cyanobiphenyl (8CB) molecules in prewetting films spreading on silicon wafers covered by a thin native oxide layer. When the macroscopic part of the drop is in the smectic phase, 8CB partially wets the substrate, and we observe the spreading of a nondense monolayer in front of a 45-Å-thick homogeneous film. Those two films are of great interest because they appear during the spreading of all *n*CB compounds ($4<n<12$, *n* being the length of the alkyl tail of the LC molecule) both in the nematic and in the smectic phases [7]. By ellipsometry, we show that the density of the monolayer depends on the relative humidity and that the homogeneous film may be similar to the trilayer observed in Langmuir films of the same compound [13,14]. A careful study of x-ray reflectivity spectra allows us to confirm this trilayer organization and to determine precisely the substructure of this film. According to [15], we discuss the origin of the stability of the trilayer stacking in terms of dipolar interaction. Finally, we study the shape of a drop spreading in the nematic phase, where 8CB completely wets the substrate. We observe a complex structuration of the drop close to the solid substrate. The specific spreading behavior of the trilayer is of particular interest since it may result from the dipolar interactions that are believed to account for the stability of this film.

Even though using silicon wafers as substrates ensures very good contrast for x-ray studies [17], the determination of the arrangement of the LC molecules in films that are thinner than 50 Å has proved to be tricky. One common approach to fitting complex x-ray reflectivity data (meaning data that cannot be described by a one-slab model, which can be solved analytically) is to use at least two different physical models or two different fitting procedures in order to validate one solution. For our analysis, we use the slab and finite element models concurrently. The detailed analysis of the corresponding fitting procedures is presented in an appendix.

II. EXPERIMENTAL DETAILS

The liquid crystal used was 8CB from BDH (Merck). The purity as provided by the manufacturer is better than 99.5% 8CB forms a smectic-A_d phase (smectic phase where the molecules organize in bilayers, with their long axis along the normal of the bilayers) between 21.5 and 33.5 °C, a nematic phase between 33.5 and 40.5 °C, and an isotropic phase

above 40.5 °C [18]. All phases consist of rodlike molecules organized in ''dimers'' [19] with a rigid polar center formed by the overlapping cyanobiphenyl groups and one flexible alkyl chain extending on each side of the dimer. The director of the liquid crystalline phases is along the long axis of the dimers. The length of one monomer is 22 Å [20], and the smectic periodicity is 31.4 Å [21], corresponding roughly to the length of the dimers.

The substrates were silicon wafers [2 in. diameter, intrinsic, orientation (100), purchased from Siltronix] covered by native oxide. Using ellipsometry, we found the thickness of the oxide to be 15–25 Å, with the uncertainty due to variation between wafers. To remove organic contaminants we cleaned the substrate using UV illumination under oxygen [22]. Additionally, during the last 20 min of cleaning, we switched the UV lamp off and swept the substrate with a flow of oxygen saturated with water. This ensured that available silanol groups were covered with water and therefore largely protected from ambient contamination. We used atomic force microscopy and x-ray reflectivity to check that this cleaning procedure does not increase the roughness of the substrate. Using x-ray reflectivity, we measure that the roughness of the wafers varies between 3 and 4.5 Å depending on the wafer [cf. Appendix, Sec. 2 for a definition of the roughness].

In order to get prewetting film areas that were larger than the footprint of the x-ray beam (1 mm×26 mm at the critical angle), we deposited lines ($V \approx 1\ \mathrm{mm}^3$) of 8CB on freshly cleaned silicon wafers using a copper wire stretched between two electrical tweezers held by the arm of a micromanipulator. These lines were typically 4 cm long and 1 mm wide. We allowed them to spread at room temperature under ambient atmosphere for at least 1 day to make sure that the prewetting film extended over more than 1 mm [Fig. 3(b)].

The x-ray generator (Rigaku RU-200BEH) is a rotating anode operating at 40 kV and 25 mA with a copper target and a fine focus (0.1 mm×1 mm). The apparent source is a point (0.1 mm×0.1 mm), and the scattering plane is horizontal. A germanium (111) monochromator is used to select the Cu $K\alpha_1$, line ($\lambda = 0.15405$ nm). We use a slit before the sample with size of 0.1 mm×1 mm. The intensity of the incident beam is 610 000 count/s with a background scattering of the order of 0.08 count/s. The reflected beam is detected by a scintillation detector. A slit (0.5 mm) in front of the detector and at a distance of 320 mm from the sample defines the resolution of the scattered beam.

We used a spatially resolved ellipsometer to observe the spreading of the film before x-ray reflectivity measurements. This setup has been described elsewhere [23].

III. BASIC EQUATIONS AND ORDERS OF MAGNITUDE

A. X-ray reflectivity

Although the x-ray wavelength λ is comparable to atomic dimensions and thus to the roughness of the interfaces, specular x-ray reflection can be described by the Fresnel laws of classical optics [24]. For x-rays, the refractive index is given by

$$n = 1 - \delta - i\beta, \tag{1}$$

where $\delta = \lambda^2 r_0 \rho / 2\pi (\sim 10^{-6})$, r_0 is the classical electron radius ($r_0 = 2.85 \times 10^{-15}$ m), λ is the wavelength of the beam ($\lambda = 1.54$ Å), ρ is the total electron density, and $\beta = \lambda / 4\pi\mu$, where μ is the x-ray absorption length ($\beta \sim 10^{-8}$).

X-ray reflectivity measures the ratio $I(\theta)/I_{\mathrm{incident}}$, where $I(\theta)$ is the intensity of x rays that are reflected in the specular direction from a surface as a function of the angle θ between the incident beam and the plane of the sample, and I_{incident} is the intensity of the incident beam. The reflectivity of a bare, perfectly smooth substrate with a sharp interface with vacuum is the Fresnel reflectivity R_F. In the kinematic approximation, the reflectivity of a real surface and of a surface covered by a film may be expressed as a perturbation of the Fresnel reflectivity:

$$R(Q) = R_F(Q) |\Phi(Q)|^2, \tag{2}$$

$$\Phi(Q) = \frac{1}{\rho_\infty} \int_{-\infty}^{+\infty} \left\langle \frac{d\rho(z)}{dz} \right\rangle \exp(Q_z . z)\, dz, \tag{3}$$

where $Q_z = (4\pi/\lambda)\sin(\theta)$ is the scattering vector, $\langle d\rho/dz \rangle$ is the derivative of the electron density profile averaged over the in-plane coherence length of the x rays, and ρ_∞ is the density of the semi-infinite substrate.

Equations (2) and (3) describe the interference pattern that results from the reflection of x rays from an arbitrary electron distribution $\rho(z)$. Therefore, the interpretation of the measured x-ray spectra is based on finding proper electron density profiles whose reflectivity properties best match the measured data.

Before describing this method and the model we used for electron density profiles, let us discuss three relevant parameters of the experiment.

(i) The reflectivity is expressed as the Fourier transform of the gradient of the electron density along the substrate normal. Therefore, the maximum value of scattering vector $Q_{\max}$ gives an order of magnitude for the sensitivity of the technique to modulations of the electron density profile. $d_{\min} = \pi / Q_{\max}$ is the theoretical spatial sensitivity of the experiment: it provides an estimate of the minimum length that can be observed in the electron density profile. $Q_{\max}$ is limited by the signal over noise ratio of the setup, which depends on the x-ray source, on the detector, and on the sample. In our experiment, $d_{\min}$ is of the order of 5 Å.

(ii) The in-plane coherence length ξ of the x ray over which the gradient of the electron density is averaged. ξ gives the maximum wavelength for the roughness of the interfaces that can be measured. In our experiment, this length is of the order of 10^4 Å.

(iii) As discussed in detail by Pershan [25], another important parameter is the characteristic length $L^{-1} = \lambda^{-1} \sqrt{|\chi(-\infty)|}$, where $\chi(-\infty)$ is the dielectric susceptibility of the substrate. It corresponds to the minimum film thickness over which one would be able to get the phase information contained in Eq. (3). Therefore, L provides an estimate of the minimum thickness of the film for which analysis of x-ray data using the Parrat method can differentiate between an electron density profile and the corresponding reflected profiles [$\langle d\rho(z)/dz \rangle = -\langle d\rho(z_0 - z)/dz \rangle$,

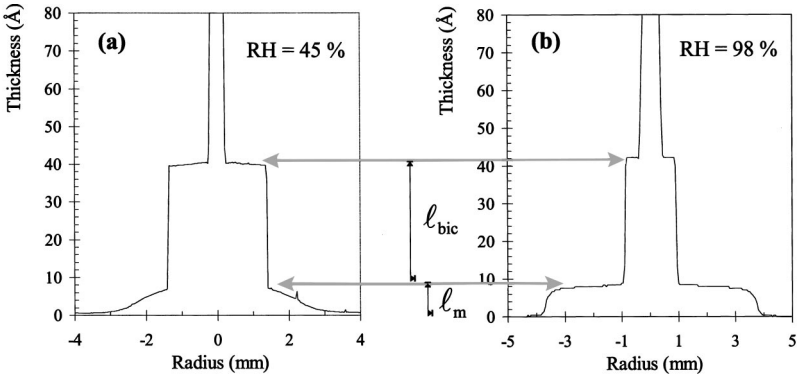

FIG. 1. Ellipsometric profiles of two 8CB drops spreading at room temperature. (a) Relative humidity (RH) = 45%, (b) RH = 98%. The data are not filtered. The thickness is deduced from the retardation (raw data) assuming a constant optical index of 1.6.

where z_0 is an arbitrary plane]. In our system, L is of the order of 500 Å: therefore, we are not able to reach such precision.

Although Eqs. (2) and (3) are useful to discuss the relevant parameters of the experiment, we do not use them to describe our experimental data. As explained in the Appendix, we use a matrix formulation equivalent to Parrat's formulation [26].

B. Ellipsometry

The spatial resolution of the ellipsometer is 20 μm. It is sensitive to thickness within 1 Å. However, one must be careful because ellipsometry is not convenient for measuring the absolute thickness of such films since they are birefringent and we do not know if the optical indexes in molecularly thin layers are equal to the bulk optical indexes. Additionally, it is not possible to decorrelate the thickness from the optical index value for very thin films ($t < 200$ Å).

IV. MONOLAYER AND TRILAYER

A. Influence of humidity and temperature

Figure 1 presents two characteristic ellipsometric profiles of 8CB microdrops spreading at room temperature under (a) ambient humidity (RH$\sim$45%) and (b) saturated humidity (RH$\sim$98%). At this temperature, the macroscopic part of the drops (which are out of scale in Fig. 1) are in the smectic-A_d phase and do not spread. However, we observe the spreading of two prewetting films (partial wetting regime). Under ambient humidity [Fig. 1(a)], we observe a film with an optical thickness varying continuously from 0 to $l_m = 10 \pm 2$ Å spreading in front of a homogeneous film. Both films extend over millimeters after 3 days of spreading. The gradient of the outer film could be related to a density or tilt gradient. When the drop spreads under saturated humidity [Fig. 1(b)], we observe that the outer film has a constant thickness equal to l_m. On both profiles, the height of the edge separating the outer film from the homogeneous film is $l_{bic} = 33 \pm 2$ Å, close to the bulk smectic periodicity of 8CB [21].

The comparison between Figs. 1(a) and 1(b) indicates that the outer film is a monolayer. From the value of l_m, we can determine an order of magnitude of the tilt of the molecules in this layer: $\theta = \arccos(l_m / l_{8CB}) = 63° \pm 6°$ (assuming a rodlike model for the molecules, l_{8CB} being the length of one 8CB molecule). The origin of the appearance of a dense monolayer under a very humid environment remains unclear. As a matter of fact, we are not able to determine whether it is related to the relative kinetics of spreading of the monolayer and the dense film (water molecules have been shown to reduce the friction between a polymer film and a silicon substrate [27]) or to a thermodynamical stabilization of this film by the presence of water molecules [13].

8CB forms bilayers composed of dimers perpendicular to the layers in the smectic-A_d phase. Because the height difference we measure at the step separating the monolayer from the homogeneous film is close to the smectic periodicity of the bulk material, we think that this homogeneous film corresponds to a trilayer where a smecticlike bilayer stands on the monolayer described previously. A similar organization of 8CB molecules has been previously observed in Langmuir films of this compound [13,14].

The spreading of a trilayer is indeed observed with all of nCB compounds ($4 < n < 12$), even those that do not have a smectic phase (cf. [7]). Therefore, the trilayer appears to be induced by short-range interactions with the substrate rather than being the expression of the smectic character of 8CB. In order to illustrate this idea, we have studied the stability of this film with temperature. Figure 2 shows the range of temperature over which the ellipsometric thickness of the trilayer is constant within 0.5 Å. We have been limited in the low-temperature side by the condensation of water on the substrate below 5 °C. Above the nematic-isotropic bulk temperature transition, the trilayer dewets slowly (several hours before the appearance of the first hole at $T = 50$ °C). Therefore, the reported thickness corresponds to the metastable trilayer before it dewets. We observe that the thickness of the trilayer is constant over a wide range of temperature covering all the mesophases of the bulk compound, confirming that this structure is stabilized by short-range interaction.

In conclusion, we distinguish two different prewetting films with a height difference close to the smectic periodicity of the bulk material. The outer film is a monolayer with tilted molecules whose density depends on the relative humidity. We propose that the homogeneous film corresponds to a trilayer organization of 8CB similar to what has been ob-

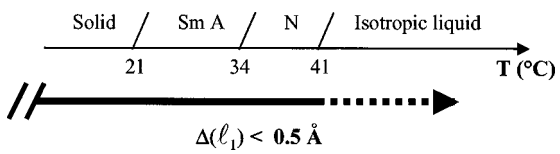

FIG. 2. Temperature domain where the trilayer has a constant thickness (within 0.5 Å) reported along with the bulk phase diagram of 8CB for comparison. The dashed line indicates a range of temperature where the trilayer is metastable (cf. text).

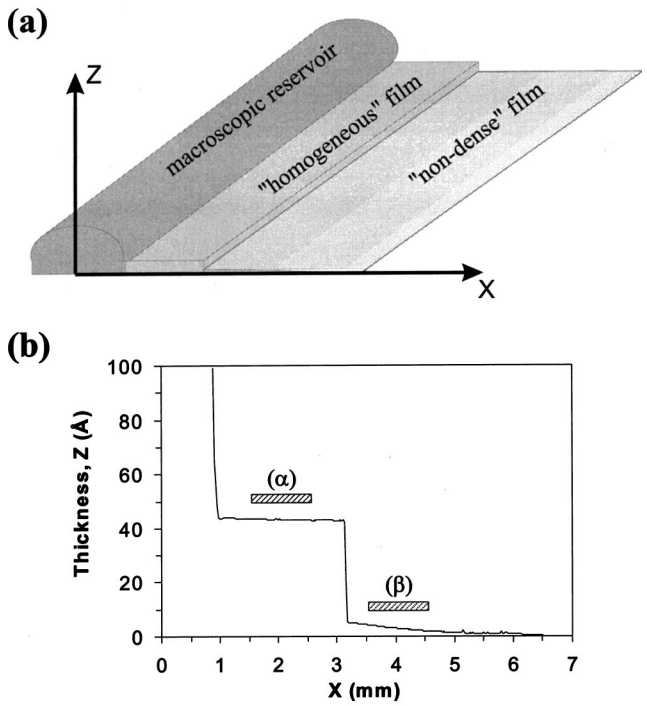

FIG. 3. (a) Sketch of the spreading geometry: the macroscopic reservoir is a ribbon of roughly 4 cm×1 mm; the prewetting films spread in front of the reservoir and extend over a couple a millimeters after 1 day of wetting at room temperature. (b) Thickness profile measured by ellipsometry along a line perpendicular to the ribbon (x direction). The thickness is measured assuming an average optical index of 1.6 for the LC film. The same sample was used to perform the x-ray experiments presented in Fig. 4. The position of the beam corresponding respectively to Figs. 4(a) and 4(b) are denoted (α) and (β), respectively, in this figure.

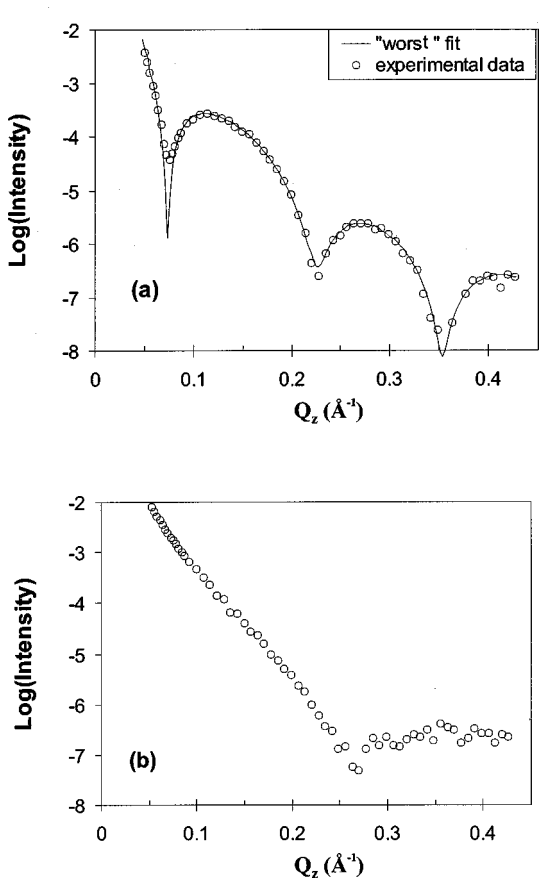

FIG. 4. (a) Symbols: x-ray reflectivity data measured on the ''homogeneous'' (trilayer) prewetting film The sample was positioned in order to have the footprint of the x-ray beam in the position (α) pictured in Fig. 1. Line: fit of the data corresponding to the worst χ^2 among all our ''mathematical solutions.'' (b) X-ray spectrum recorded on the ''nondense'' film: footprint of the beam in the position β pictured in Fig. 3.

served in Langmuir films. In order to support this idea, we have performed x-ray reflectivity experiments on these two films.

B. X-ray reflectivity

1. Experimental data and qualitative analysis

Figure 3(a) presents the geometry of the liquid crystal line we have used in order to get large-areas prewetting films. Figure 3(b) shows the ellipsometric profile of the line after 4 days of spreading at room temperature under ambient humidity. Using ellipsometry, we checked that prewetting films obtained from the drop and the line geometries are the same.

Figure 4 presents x-ray spectra obtained on different areas of the LC line. The positions of the beam corresponding to those measurements are presented in Fig. 3(b).

Figure 4(a) corresponds to measurements performed on the ''homogeneous film'' [position α in Fig. 3(b)]. The sample is mechanically positioned to have the x-ray beam incident on the area where we observed the ''homogeneous'' film by ellipsometry just before we put the sample on the stage of the x-ray setup. To make sure that the footprint of the beam is confined to this film, we check that the x-ray spectrum does not change when we move the sample (by half-millimeter steps in both directions along the x axis).

Figure 4(b) presents the data measured on the ''nondense'' film [position β in Fig. 3(b)]. The estimated position of the beam for this measurement is presented in Fig. 3(b), the maximum error for that position being 0.5 mm.

As expected from an organic film on a silicon substrate, we observe Kiessig fringes [Fig. 4(a)]. These fringes arise from interference between light reflected at the surface of the film and at the solid surface (native oxide layer). The position of the first minimum is $Q=0.075\,\text{Å}^{-1}$. Closer examination of the reflectivity reveals that minima at larger angles do not occur at positions that are integral multiples of the position of the smallest-angle minimum (we checked that this cannot be accounted for by refraction in the film). This shows that our data on the ''homogeneous'' film cannot be described by a one-slab model and therefore that the order of the LC molecules is high enough to produce a modulation of the electron density along the normal to the surface. Thus the total thickness of the film cannot be deduced from the position of the first minimum using the formula $l_{\text{total}}=\pi/Q_{\text{min}}$. Nevertheless, this equation gives a first estimate of this thickness $l_{\text{total}}=42\,\text{Å}$. Furthermore, with our experimental setup, we cannot measure reflectivity smaller than 10^{-8}, which limits our measurements to transferred vectors smaller than $Q_{\text{max}}=0.45\,\text{Å}^{-1}$, giving the resolution $d_{\text{min}}\sim 7\,\text{Å}$.

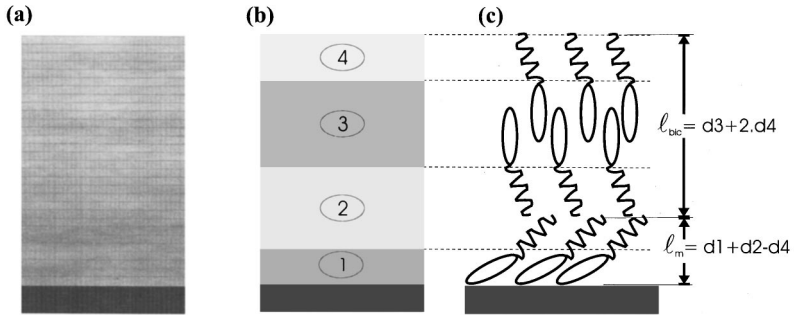

FIG. 5. (a) Sketch of the finite-element model: the film is divided into 25 layers of equal thickness and adjustable electron density. (b) The four-slab model: the film is divided into four slabs with adjustable thickness and electron density. A given slab describes a sublayer of the film with constant electron density that is associated with some specific chemical group of the 8CB molecule (polar head with high electron density and alkyl tail with low electron density). (c) Sketch of the trilayer arrangement of the LC molecules as it has been described by other groups working on Langmuir films [13,14].

The density of the monolayer over area β can be estimated by dividing the average ellipsometric thickness of this area [cf. Fig. 3(b)] by l_m. It is of the order of 40% of the density of the homogeneous monolayer. The x-ray spectrum measured in this area, presented in Fig. 4(b), exhibits only one minimum corresponding to Kiessig fringes. The position of this minimum is $Q=0.268\,\text{Å}^{-1}$. It gives us an estimate of the thickness of the ''nondense'' film in the area illuminated by the beam $l_{\text{nondense}}\sim 12\,\text{Å}$. This value is close to the value of l_m measured by ellipsometry on the homogeneous monolayer [cf. Fig. 1(b)], showing that the tilt of the molecules in contact with the substrate does not depend on the density and is equal to $57°\pm 3°$ [according to our x-ray analysis; cf. Sec. 6(b) of the appendix]. Furthermore, these results indicate that the gradient of optical thickness observed in the monolayer under ambient humidity [cf. Fig. 1(a)] is due to a decrease of the density of the monolayer as we go far from the macroscopic reservoir. Considering that we did not observe any dense substructures by antiferromagnetism on this nondense monolayer [28] and that Daillant *et al.* did not detect this film using Brewster angle microscopy [6], we conclude that the LC molecules in the nondense monolayer have a two-dimensional (2D) gaslike organization.

2. Organization of the molecules in the trilayer

We have seen in the previous section that it is not possible to use a one-slab model to describe the experimental data obtained on the ''homogeneous film'' because of the modulation of the electron density in the film. In order to describe this modulation, we have used two different models of the electron density that are presented in Fig. 5 along with a schematic representation of the trilayer organization. The multislab model [Fig. 5(b)] describes the system by using slabs of different electron density corresponding to different parts of the LC molecules. This model has been successfully used to study molecular ordering in Langmuir-Blodgett films [29], at the surfaces of bulk LC's [30], and in freely suspended LC films [31]. For our system, the alkyl tail of 8CB has a lower electron density than the polar head. Therefore, we use different slabs to describe these chemical groups. The finite-element model [Fig. 5(a)] allows one to deduce an electron density profile from the x-ray data by arbitrarily dividing the film into numerous sublayers that are thin compared to any parts of the LC molecule and to the theoretical resolution of the experiment ($\pi/Q_{\max}$). Therefore the multislab model is more directly linked to the way LC molecules are organized in the film than the finite-element model. We would like to emphasize that we do not introduce any correlation between the different slabs of the multislab model. Particularly, the electron density of each slab is fitted independently. Consequently, even if it may describe a trilayer organization, as depicted in Fig. 5, the four-slab model does not correspond intrinsically to this kind of organization. For instance, one of the conditions for this model to describe a trilayer is that the two slabs corresponding to alkyl parts (slabs 2 and 4) reach similar electron density values. We will show in the following that this condition is verified.

We cannot use these two models separately to calculate directly the electron profile in the film because the substructures arising from the modulation of the electron density, in other words, the slab thickness, are comparable to the resolution of our setup. Thus the finite-element model, which has more degrees of freedom than the multislab model, can reach different mathematical solutions, but always with the correct total thickness because this thickness is one order of magnitude larger than the theoretical resolution. In contrast, the multislab model, which can be seen as a more constrained model, may converge toward mathematical solutions even at the cost of a poor evaluation of the film thickness. In order to precisely characterize these processes, we have systematically observed the mathematical solutions that we reach when we vary the initial parameters of the fit, assuming the physical solution is one of the mathematical solutions. This analysis is presented in detail in the Appendix.

The main conclusions of this analysis are that the finite-element model allows us to determine accurately the total thickness of the film, while the multislab model allows us to describe the organization of the molecules in the film once the total thickness is known. The electron density profiles determined by the fitting procedures using both models are presented in Fig. 6. The thickness of the bilayer $l_{\text{bic}}=33^{\pm 1}\,\text{Å}$ and of the monolayer $l_{\text{mono}}=12^{\pm 1}\,\text{Å}$ is determined from this study. We propose in Fig. 6 a possible arrangement of the molecules in the film corresponding to those profiles. Even if this arrangement is not unique, our results confirm the trilayer organization of the molecules. Interestingly, the tilt angle of the molecules in contact with silica within the trilayer is equal to the tilt angle determined for the molecules in the monolayer by ellipsometry and x-ray reflectivity. The thickness of the smecticlike bilayer is also in good agreement with ellipsometry measurements.

C. Comments

The trilayer organization of the 8CB molecules we observe on silica is similar to what has been reported by other

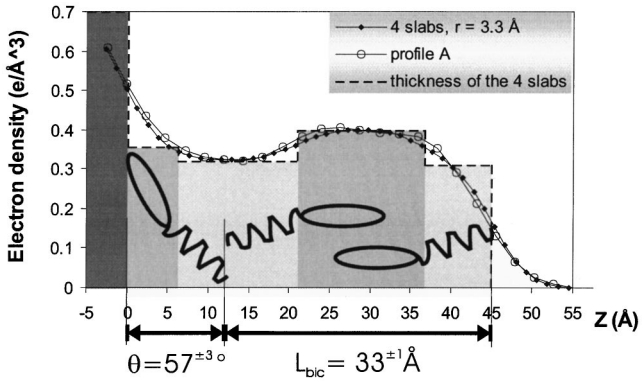

FIG. 6. Electron density profiles corresponding to solution *A* and *C* (with interfacial roughness equal to 3.3 Å for solution *C*) and sketch of a possible molecular arrangement in the trilayer that can be deduced from those profiles. The x-ray analysis allows us to determine accurately the thickness of the smecticlike bilayer (33 ± 1 Å) and the thickness of the polar monolayer (12 ± 1 Å). From these results, we can then propose several different molecular organizations of the LC molecules in the trilayer that match these values, but we cannot distinguish between them from our experimental data.

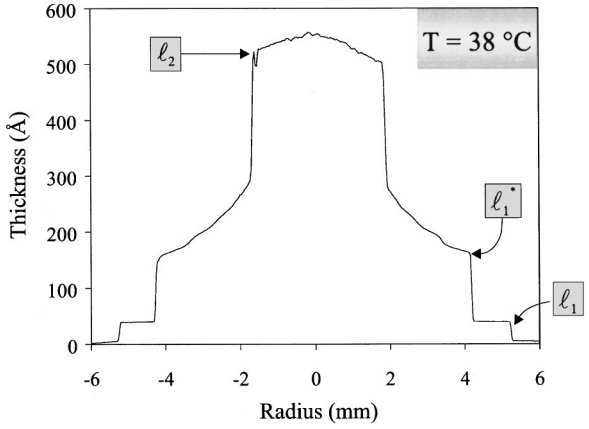

FIG. 7. Ellipsometric profile of a 8CB drop spreading in the nematic phase ($T = 38\,°C$) under ambiant humidity. In this phase, 8CB completely wets the substrate and the characteristic thicknesses that appear in the profiles indicate a (metastable) structuration of the drop.

groups on Langmuir films [13–16]. Early work on 8CB Langmuir films [13] suggested that water coming from the subphase could play a determining role in the stability of the trilayer. Since the prewetting films we observe are equilibrium structures on silica, our results show that a large amount of water is not required to produce such a trilayer organization. The formation of a stable polar monolayer at a hydrophilic interface can be understood because (1) there are strong interaction between the polar heads of the LC molecules and silica and (2) the presence of a solid surface induces a symmetry breaking which is favorable to the formation of a polar monolayer regardless of the nature of the surface [32]. The presence of a smecticlike bilayer on top of this polar monolayer is interesting because most simple liquids and light polymers form monolayers or ''Maya-like'' pyramids when they spread [23]. To our knowledge, the only reported exception is the case of ''superspreaders'' spreading on hydrophobic surfaces (formation of bilayers) [33]. In the case of Langmuir films, there is strong experimental evidence [15,16] that the trilayer organization is energetically favored by the presence of a smecticlike bilayer. The bilayer allows the film to compensate for the overall dipole of the polar monolayer if there is an excess of molecules having their dipoles pointing upward in the bilayer. We think this model is also applicable to our system.

In order to illustrate the specificity of the smecticlike bilayer forming the trilayer, we present in Fig. 7 a typical ellipsometric profile of a 8CB drop spreading in the nematic phase. In this phase, 8CB completely wets the substrate and we observe three characteristic thickness in the profile, l_1, l_1^*, and l_2. Here l_1 is the thickness of the trilayer. l_2 has been interpreted as a metastable thickness resulting from the competition between spreading energy and elastic distortions in the drop (cf. [7]). The thickness l_1^* is equal to the thickness of the trilayer plus an integral multiple of the smectic periodicity of 8CB. The corresponding number of smectic bilayers is between 3 and 5, and does not depend on temperature in the whole nematic range. The existence of the smectic block l_1^* is related to the surface induced ordering effect [3]. The fact that l_1^* is constant with temperature remains to be clarified. However, in the following, we will only focus on the dynamical behaviors of these smectic layers. All the ellipsometric profiles we have observed in the nematic phase have two common features: (i) the trilayer spreads faster than the smectic block, and (ii) bilayers of Nos. 2, 3, and 4 form a compact block that spreads at a given speed. This shows that the first smecticlike bilayer, which is part of the trilayer film, has a specific behavior. According to de Gennes and Cazabat [34], assuming that each layer is an incompressible two-dimensional liquid, a group of layers having the same velocity indicates that the chemical potential of the molecules is equal in every layer forming that group. Therefore, the chemical potential of the smecticlike bilayer that stands directly on the polar monolayer is different from the potential of all the successive bilayers forming the bloc l_1^*. The specificity of the first bilayer may be due to an excess of dipoles pointing up that compensates for the polarity of the monolayer, supporting the model proposed by Ibn-Elhaj *et al.* [15].

V. CONCLUSION

We have studied the organization of 8CB at the vicinity of the surface of a silicon wafer by observing the wetting of microdrops at different temperatures and relative humidity rates.

In the smectic phase, 8CB partially wets the substrate and we observe the spreading of two prewetting films. Combining ellipsometry and x-ray reflectivity, we have shown that these films correspond to a monolayer and a trilayer.

(i) The LC molecules are tilted in the monolayer. Under ambient humidity, this film exhibits a gradient of density along the drop radii, but the tilt of the molecules does not depend on the density. We think that 8CB molecules organize in a 2D-gas-like structure when the monolayer is nondense.

The trilayer film is formed by a smecticlike bilayer standing above a monolayer with tilted molecules in contact with

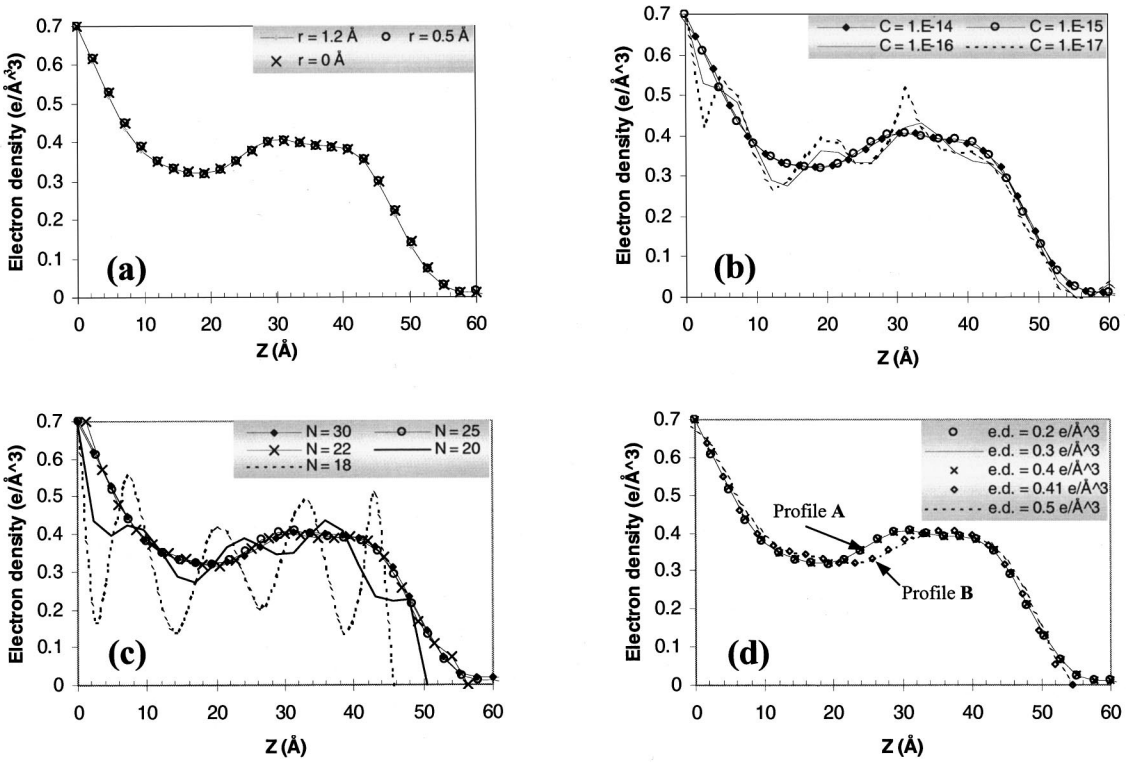

FIG. 8. Evolution of the electron density profiles calculated with the finite-element model when (a) the interfacial roughness is changed. We assign the same roughness for all sublayer interfaces, at the free surface of the film and at the surface of the silicon wafer. (b) The constraint, which is a numerical parameter that limits the variation of the electron density from one sublayer to the other, is modified. (c) The number of sublayers, which have a thickness fixed to 2.4 Å, is increased. (d) The initial electron density of the sublayers is varied (all the sublayers have the same electron density when we start a fitting procedure).

the substrate. The tilt angles in the monolayer and in the trilayer (for the molecules in contact with the substrate) are the same ($\theta = 57^{\pm 3}°$). We think that the stability of the trilayer results from dipolar interaction between the bilayer and the monolayer.

In the nematic phase, 8CB completely wets the substrate. During the spreading of a drop, we observe the appearance of a smectic block, between three and five smectic bilayers thick, above the trilayer. The relative spreading dynamics of this block and of the trilayer indicates that the smecticlike bilayer that is part of the trilayer exhibits some specific interaction with the substrate (covered by the monolayer). We think that this specificity results from the dipolar interaction mentioned above.

ACKNOWLEDGMENTS

The authors are grateful to J. Maclennan and D. Coleman for a careful reading of the manuscript. One of them (S.B.) thanks Thomson-CSF for financial support.

APPENDIX: FITTING PROCEDURES AND MODELS

1. Fitting procedure

We use a matrix formulation to fit our experimental data because it is convenient to compute and does not use the kinematic approximation. The main drawback of this technique is that it does not use any analytic form of the electron density profile. Briefly, we calculate the reflectivity of a model electron profile. This profile contains adjustable parameters that are used to minimize the absolute difference between the calculated reflectivity and the measured reflectivity using the Levenberg-Maquart fitting routine.

We also calculated the Patterson function of our x-ray spectra, but our films are too thin to deduce precisely their thickness by using this method.

2. Interfacial roughness

We model the interfacial roughness by Gaussian functions such as

$$\left\langle \frac{d\rho}{dz} \right\rangle \propto \frac{\exp(-z^2/2r^2)}{(2\pi r^2)^{1/2}},$$

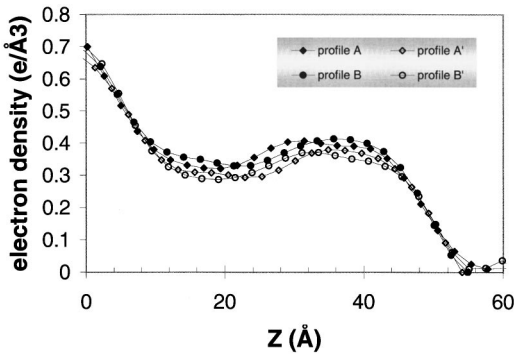

FIG. 9. Electron density profiles corresponding to the solutions A and B (solid symbols) and corresponding symmetrical profiles A' and B'; cf. text (open symbols).

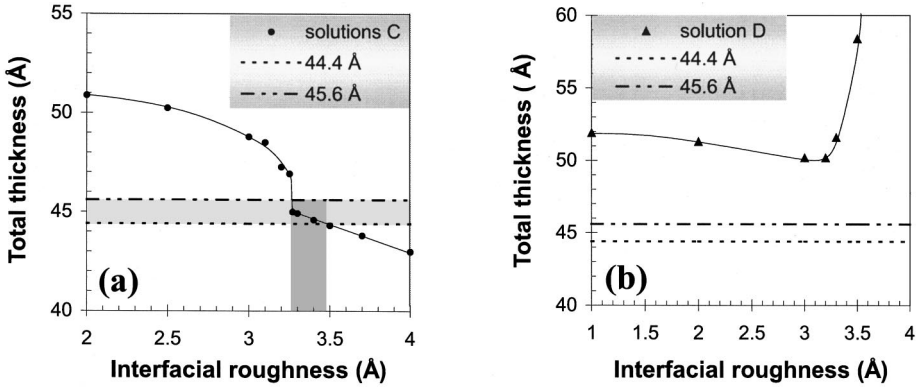

FIG. 10. Variation of the total thickness of the trilayer corresponding to the electron density profiles calculated with the four-slab model as a function of the interfacial roughness. We assign the same roughness for all slab interfaces, at the free surface of the film and at the surface of the silicon wafer. (a) Profiles corresponding to solution *C*. (b) Profiles corresponding to solution *D*. The dashed lines define the domain $L_{\text{total}}=45\pm0.6$ Å that is physically acceptable according to the analysis carried with the finite-element model [cf. Sec. 6 b of the Appendix]. This criterion allows us to exclude solution *D* and determine a roughness domain for which the electron density profiles of type *C* can have a physical meaning as depicted by the gray boxes in this figure.

where r is the root-mean-square roughness of the interface. In our analysis, we set all the interfacial roughnesses to the same value. This is reasonable approximation because the films we observed are of molecular thickness. We have used atomic force microscopy to ensure that the roughness of the free surface of the film and of the substrate are indeed conformal [28].

3. Definition of a solution

As a result of the large number of fitting parameters and the loss of any phase information (discussed in Sec. III A), the solution to the inversion of the experimental data is not unique. The problem is then to determine which is the physical solution among all mathematical solutions. A mathematical solution is an electron profile that describes experimental data ''perfectly.'' That is, the calculated reflectivity from this profile is equal to the experimental data within the experimental error. Figure 4 presents the experimental data and the calculated reflectivity for the worst fit (in terms of χ^2) in this study.

4. Models of the electron density

The two models we use to describe the modulation of the electron density in the trilayer are depicted in Fig. 5 and explained in the text. The ''finite-element'' model uses many slabs (25) of the same thickness and gives an envelope of the electron density profile. The four-slab model use four slabs that correspond to different sublayers within the films composed by the same chemical groups (alkyl tail or polar head). It gives the organization of the molecules in the trilayer.

5. Finite-element model

a. Mathematical solutions

In order to exclude solutions that do not have physical meaning, it is necessary with this model to introduce a parameter (the ''constraint'') that limits the gradient of the electron density from one layer to another.

Figure 8 presents the variation of the electron density profile when the interfacial roughness [Fig. 8(a)], the constraint [Fig. 8(b)], number of layers [Fig. 8(c)], and the initial electron density [Fig. 8(d)] are modified. For the sake of clarity, we have not presented all the profiles we have calculated in this figure. As expected, we observe in Fig. 8(a) that the

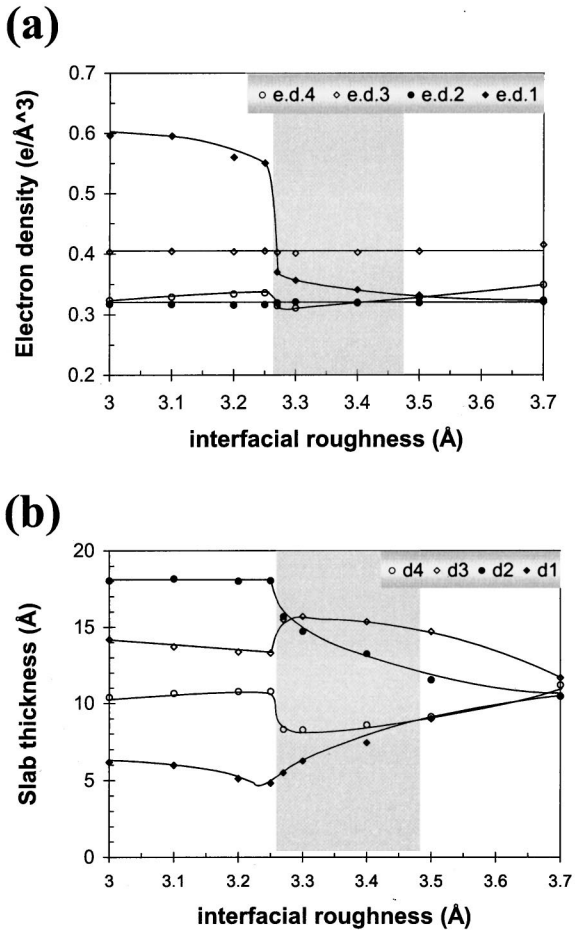

FIG. 11. Evolution of the parameters [electron density of the slabs (a) and thickness of the slabs (b)] of the profiles corresponding to solution *C* with the interfacial roughness. The gray boxes indicate the interfacial roughness domain corresponding to solutions that are physically acceptable according to $l_{\text{total}}=45\pm0.6$ Å (cf. Fig. 10).

TABLE I. Parameters of the solution *C* as determined from Fig. 11. The thicknesses of the smecticlike bilayer and the monolayer are calculated from those parameters according to the formula given in Fig. 5.

Solution *C*	Slab 1	Slab 2	Slab 3	Slab 4	Bilayer	Monolayer	Total
Thickness (Å)	7 ± 2	14 ± 3	15 ± 1	9 ± 1	33 ± 1	12 ± 1	45 ± 1
Density ($e/\text{Å}^3$)	$0.40^{\pm0.06}$	$0.32^{\pm0.01}$	$0.40^{\pm0.01}$	$0.32^{\pm0.01}$		$\theta=57\pm3°$	

interfacial roughness has no influence on the calculated electron density profile. We observe in Fig. 8(c) that the fit does not correspond to a physical solution (infinite electron density gradient at the interface LC/air) when the number of layers is too small. Once we use enough layers, the calculated profiles do not depend on this parameter. Figure 8(b) shows that a large value for the constraint prevents convergence toward nonphysical solutions (oscillation of the electron density with a small spatial periodicity) and that it has no effect on the profile when it is increased further. Finally, we observe in Fig. 8(d) that we can reach either ''solution *A* profiles'' (respectively, ''solution *B* profiles'') when the electron density is initially set below $0.40\,e/\text{Å}^3$ (respectively, above $0.40\,e/\text{Å}^3$) before starting the fitting procedure.

As discussed by Pershan [25], the electron density profiles that can be extracted from x-ray reflectivity measurements are not unique because the equations of x-ray reflectivity are invariant by an inversion operator that changes the density ρ to $(\rho_{\text{substrate}}-\rho)$ and the coordinate z to $(L_{\text{total}}-z)$. Usually, physical arguments allow one to choose between the two possible profiles. In our case, solution *A* is not related to solution *B* by the symmetry of this operator. Thus we have four possible profiles (A,B,A',B', where A' and B' are the symmetric solutions of *A* and *B*, respectively) and no clear physical arguments to exclude any of them. Figure 9 presents the four A,B,A',B' solutions. We observe in this figure that the four profiles correspond to the same total thickness of the film. However, they are different and the exact electron density profile cannot be determined using this model.

b. Film thickness

For a given electron density profile, there are two ways to measure the total film thickness.

(i) The first consists in measuring the distance that separates the abscissa of the points that have electron density equal to $\langle\rho\rangle/2$ and $(\rho_{\text{substrate}}+\langle\rho\rangle)/2$ corresponding, respectively, to the LC/air and substrate/LC interfaces ($\langle\rho\rangle$ is the average density in the film). This method does not make any assumption about the organization of the molecules in the film. The result is a thickness of 44.6 ± 0.2 Å.

(ii) The second is linked to the trilayer model and takes the LC/air and substrate/LC interfaces at the abscissa corresponding to density equal, respectively, to $\rho_{\text{min}}/2$ and $(\rho_{\text{substrate}}+\rho_{\text{max}})/2$. With this model, the thickness is 45.4 ± 0.2 Å. As will appear in the following, this approach is more suitable for comparison between the total thickness determined using this model and using the multislab model.

Combining these two approaches, we conclude that the total thickness of the homogeneous film is equal to 45 ± 0.6 Å.

6. Multislab model

a. Mathematical solutions

Before going any further, we would like to emphasize that we do not introduce any correlation between the different slabs in this model. Particularly, the electron density of each slab is fitted independently. Consequently, the four-slab model does not correspond intrinsically to a trilayer organization. For instance, one of the conditions for this model to describe a trilayer organization is that the two slabs corresponding to alkyl parts (slabs 2 and 4) reach the same electron density. We will show in the following that this condition is verified.

Using the same method as described in Sec. 5 of the appendix, we systematically run our fitting procedures with the four-slab models to study the possible mathematical solutions. We observe that we reach two types of solutions, *C* and *D*, depending on the values of the initial parameters. Contrary to what has been observed using the finite element model (where the value of the initial electron density determines which solution, *A* or *B*, is reached), we cannot find a specific parameter that determines which solution is reached. Furthermore, we observe that, for a given type of solution, the profile is stable when the initial thickness and density of the slabs vary. In contrast, the profile changes when the interfacial roughness changes.

b. Physical solution

The next step is to use the value of the total thickness of the film, l_{total}, that has been determined using the finite element model [Sec. 5(b) of the appendix] to select from all the density profiles corresponding to solutions *C* and *D* those that effectively fulfill the constraint $l_{\text{total}}=45\pm0.6$ Å. Figure 10 shows the evolution of the total thickness of the profiles corresponding to solutions *C* and *D* as a function of the interfacial roughness. We observe in this figure that the thickness constraint rules out solution *D*, but not solution *C*, which is still valid for roughness between 3.26 and 3.48 Å. Such precision in the value of the roughness has no physical meaning. Physically, this result indicates that the roughness of the substrate and the free surface of the film are both of

TABLE II. Parameters of the solution C' symmetrical profile of solution *C*.

Solution C'	Slab 1	Slab 2	Slab 3	Slab 4	Bilayer	Monolayer	Total
Thickness (Å)	9 ± 1	15 ± 1	14 ± 3	7 ± 2	28 ± 1	17 ± 3	45 ± 1
Density ($e/\text{Å}^3$)	$0.38^{\pm0.06}$	$0.30^{\pm0.01}$	$0.38^{\pm0.01}$	$0.30^{\pm0.06}$		$\theta=46\pm3°$	

the order of 3.3 Å, which is a reasonable range compared to the typical roughness of silicon wafers (3–4.5 Å). Nevertheless, we can use the ''interfacial roughness'' as a numerical parameter and, in this frame, such precision is meaningful and necessary in order to determine the value of the other parameters of the four-slab model. Closer examination of Fig. 10 shows that the total thickness determined by this model is larger than the film thickness for $r<3.26$ Å and that it drops abruptly in the good range at $r=3.26$ Å. For $r>3.26$ Å, the variation of the four-slab total thickness is smooth.

Figure 11 shows the evolution of solution C as a function of the interfacial roughness. We observe that the electron density profile depends strongly on the exact value of the interfacial roughness. More precisely, the abrupt decrease of the total thickness at $r=3.26$ Å is associated with a drop of the electron density (e.d.) of slab 1 from a nonphysical value (e.d. $>0.55\,e/\text{Å}^3$ for $r<3.25$ Å) to a reasonable value (e.d. $=0.40\pm0.06\,e/\text{Å}^3$ for $3.26<r<3.48$).

From this result we can deduce the value of all the parameters of the four-slab models. Then we can determine the length of the smecticlike bilayer, the length of the monolayer, and the tilt angle of the LC molecules in the monolayer assuming a rodlike model (cf. Fig. 5). All these values are presented in Table I.

Qualitatively, we observe that (1) the electron density of slab 1 (respectively, slab 2) is equal to the density of slab 3 (respectively, slab 4), (2) the electron density of slabs 1 and 3 is higher than the density of slabs 2 and 4, the ratio between these densities is 1.25, and (3) the thicknesses of slabs 2 and 3 are approximately equal to 2 times the thickness of slabs 4 and 1.

From (1) and (2), we deduce that slabs 1 and 3 correspond to the polar head of the 8CB molecules and that slabs 2 and 4 describe their alkyl tail. The ratio between the head and tail densities (1.25) is close to what is obtained by assuming a rodlike shape of the LC molecules and counting the electrons in both parts. Furthermore, the polar head of 8CB is expected to be at the highly polarizable silica/LC interface and the alkyl tail at the LC/air interface. Our results agree with those constraints (slab 1 corresponds to polar head and slab 4 to alkyl tail). Finally, (3) shows that solution C describes a trilayer organization of the molecules.

Quantitatively, we observe that (1) the thickness of the smecticlike bilayer is 33 Å close to the smectic periodicity of the bulk 8CB (31.4 Å), (2) the thickness of the monolayer is 12 Å, equal to the thickness of the nondense film that spreads in front of the trilayer (cf. Sec. IV A), and (3) the tilt angle of the molecules in contact with silica is $57°\pm3°$ assuming a rodlike shape for the LC molecules.

We know from SHG experiments [8,9] that the organization of 8CB molecules on silica does not depend on the density of the monolayer or on the presence of other LC molecules on top of it. Our observation that the thickness of the monolayer is equal to the thickness of the nondense film is in good agreement with this. The tilt angle of the molecules in the monolayer is also in agreement with SHG experiments although we must be careful since SHG only probes the organization of the polar head and not of the entire molecule.

As explained in Sec. 5(a) of the appendix, there is a symmetric profile C' associated with solution C. The values of its parameters are given in Table II. Although solutions C and C' are close to each other, we think that solution C' is ruled out because the thickness of the monolayer calculated from this solution is significantly different from the thickness of the nondense film.

7. Comparison of both models

We can use solution C to determine which of solutions A,B,A',B' best describes our system. Figure 6 presents electron density profiles corresponding to solution A (which is closest to C) and C with the corresponding molecular arrangement. Note that there are several possible molecular arrangements that can be deduced from solutions C and A. Only the total thickness of the film, the length of the smecticlike bilayer, and the tilt angle of the molecules in contact with silica are relevant. We observe that the profiles corresponding to solution A (which is unique) and to solution $C(r=3.3\,\text{Å})$ are in good agreement. A relevant point is that the maximum and minimum densities, corresponding, respectively, to the polar head and the alkyl part densities, are respectively equal to 0.40 ± 0.01 and $0.32\pm0.01\,e/\text{Å}^3$ for all profiles corresponding to solution C and for the profile corresponding to solution A.

[1] P. G. de Gennes and J. Prost, *The Physics of Liquid Crystals* (Clarendon, Oxford, 1993).

[2] H. Yokoyama, *Handbook of Liquid Crystals Research* (Oxford University Press, New York, 1997), Chap. 6.

[3] B. Jérôme, Rep. Prog. Phys. **54**, 391 (1991).

[4] M. F. Grandjean, C. R. Hebd. Seances Acad. Sci. **166**, 165 (1918).

[5] P. S. Pershan, J. Phys. (Paris), Colloq. **10**, C7-1 (1989).

[6] J. Daillant, G. Zalczer, and J. J. Benattar, Phys. Rev. A **46**, R6158 (1992).

[7] M. P. Valignat, S. Vilette, J. Li, R. Barberi, R. Bartolino, E. Dubois-Violette, and A. M. Cazabat, Phys. Rev. Lett. **77**, 1994 (1996).

[8] C. S. Mullin, P. Guyot-Sionnest, and Y. R. Shen, Phys. Rev. A **39**, 3745 (1989).

[9] M. B. Feller, W. Chen, and Y. R. Shen, Phys. Rev. A **43**, 6778 (1991).

[10] J. S. Foster and J. E. Fromer, Nature (London) **333**, 542 (1988).

[11] H. Yamada and K. Nakayama, Jpn. J. Appl. Phys., Part 1 **32**, 2958 (1993).

[12] E. Matsui, K. Nito, and A. Yasuda, Liq. Cryst. **17**, 311 (1994).

[13] J. Xue, C. S. Jung, and M. W. Kim, Phys. Rev. Lett. **69**, 474 (1992).

[14] M. N. G. De Mul, J. A. Mann, Jr., Langmuir **10**, 2311 (1994).

[15] M. Ibn-Elhaj, H. Riegler, H. Möhwald, M. Schwendler, and C.

A. Helm, Phys. Rev. E **56**, 1 (1997).
[16] M. Harke, M. Ibn-Elhaj, H. Möhwald, and H. Motschmann, Phys. Rev. E **57**, 1806 (1998).
[17] P. Lambooy, Ph.D. thesis, FOM-Institut, the Netherlands, 1992 (unpublished).
[18] A. J. Leadbetter, J. L. Durrant, and M. Rugman, Mol. Cryst. Liq.. Cryst., Lett. Sect. **34**, 231 (1997).
[19] A. J. Leadbetter, R. M. Richardson, and C. N. Colling, J. Phys. (Paris), Colloq. **36**, C1-37 (1975).
[20] A. J. Leadbetter, Nature (London) **252**, 221 (1974).
[21] T. A. Krenstel, O. D. Lavrentovitch, and S. Kumar (unpublished).
[22] J. R. Vig, J. Vac. Sci. Technol. A **3**, 1027 (1985).
[23] F. Heslot, N. Fraysse, and A. M. Cazabat, Phys. Rev. Lett. **62**, 1286 (1989).
[24] J. Als-Nielsen, Physica A **140**, 376 (1986).
[25] P. S. Pershan, Phys. Rev. E **50**, 2369 (1994).
[26] L. G. Parrat, Phys. Rev. **95**, 359 (1954).
[27] S. Villette, M. P. Valignat, A. M. Cazabat, L. Jullien, and F. Tiberg, Langmuir **12**, 825 (1996).
[28] S. Bardon, M. P. Valignat, A. M. Cazabat, W. Stocker, and J. P. Rabe, Langmuir **14**, 2916 (1998).
[29] M. Ibn-Elhaj, H. Riegler, and H. Möhwald, J. Phys. I **6**, 969 (1996).
[30] X. Z. Wu, E. B. Sirota, S. K. Sinha, B. M. Ocko, and M. Deutsch, Phys. Rev. Lett. **70**, 958 (1993).
[31] S. Gierlokta, P. Lambooy, and W. H. De Jeu, Europhys. Lett. **12**, 341 (1990).
[32] M. A. Osipov, T. J. Sluckin, and S. J. Cox, Phys. Rev. E **55**, 464 (1997).
[33] F. Tiberg and A. M. Cazabat, Europhys. Lett. **25**, 205 (1994).
[34] P. G. de Gennes and A. M. Cazabat, C. R. Acad. Sci., Ser. II: Mec., Phys., Chim., Sci. Terre Univers **310**, 1601 (1990).